Plutonium oxide melt structure and covalency

Stephen K. Wilke[1,2,*], Chris J. Benmore[2], Oliver L. G. Alderman[3], Ganesh Sivaraman[4], Matthew D. Ruehl[5], Krista L. Hawthorne[5], Anthony Tamalonis[6], David A. Andersson[7], Mark A. Williamson[5], Richard Weber[1,2]

[1] *Materials Development, Inc.; Evanston, IL 60202, USA.*

[2] *X-Ray Science Division, Advanced Photon Source, Argonne National Laboratory, Lemont, IL 60439, USA*

[3] *ISIS Neutron & Muon Source, Rutherford Appleton Laboratory, Chilton, Didcot, Oxon OX11 0QX, U.K.*

[4] *Department of Chemical & Biomolecular Engineering, University of Illinois at Urbana-Champaign, Urbana, IL 61801, USA*

[5] *Chemical and Fuel Cycle Technologies Division, Argonne National Laboratory, Lemont, IL 60439, USA*

[6] *Tamalonis Technologies, Highland Park, IL 60035, USA*

[7] *Materials Science and Technology Division, Los Alamos National Laboratory, Los Alamos, NM 87545, USA*

Advances in nuclear power reactors include the use of mixed oxide fuel, containing uranium and plutonium oxides[1]. High-temperature behavior and structure of PuO_{2-x} above 1800 K remain largely unexplored[2,3], and these conditions must be considered for reactor design and planning mitigation of severe accidents. Herein, we measure the atomic structure of PuO_{2-x} through the melting transition up to 3000 ± 50 K using X-ray scattering

of aerodynamically levitated and laser beam heated samples, with O/Pu ranging 1.57 to 1.76. The fluorite PuO_{2-x} crystal phase loses oxygen upon heating, and its thermal and chemical expansion are consistent with extrapolation of prior data[4,5]. Liquid structural models consistent with the X-ray data are developed using machine-learned interatomic potentials and density functional theory. Molten $PuO_{1.76}$ contains some degree of covalent Pu-O bonding, signaled by degeneracy of Pu 5*f* and O 2*p* orbitals. The liquid is isomorphous with molten $CeO_{1.75}$, demonstrating the latter as a nonradioactive, nontoxic, structural surrogate when differences in oxidation potential of Pu and Ce are accounted for. These characterizations provide essential constraints for modeling pertinent to reactor safety design.

Nuclear energy is one of several sources that will play a key role in decarbonizing electric power generation, but longstanding challenges associated with waste management hinder its widespread use[6]. One promising advancement is the use of mixed oxide fuels (MOX) containing U, Pu, and other actinide oxides in both Gen-III and Gen-IV reactors[1]. MOX fuel can make use of Pu and other actinides recycled from the used fuel of current Gen-III reactors, improving energy utilization, reducing the amount of waste disposed in a geologic repository, and decreasing the time required for Gen-III waste isolation to 300 instead of 300,000 years[7]. MOX fuel can also provide a pathway for repurposing excess weapons-grade Pu[8,9].

Reactor design for MOX fuel relies heavily on thermochemical models that are based on experimental measurements. Yet, experimental data on thermophysical properties and chemistry of plutonium oxides are scarce above 1800 K[2,3] because of challenges working at high temperature, such as sample contamination from reactions with most crucible materials, in

addition to safety hazards of radioactivity and toxicity. PuO_2 can lose oxygen to form PuO_{2-x} above ~1000 K, with the O/Pu ratio dependent on temperature and oxygen chemical potential. No structure data are available for Pu-O solids above 1773 K[10,11]. There are no reported experimental data for the liquid[2] except for melting point, T_m, which recently was reassessed to be 300 K higher than decades' of past research had suggested[12]. Only two molecular dynamics studies have included the liquid, limited to stoichiometric PuO_2[13,14]. The paucity of experimental information on high-temperature and melting behavior of Pu-O must be addressed to enable reactor and safety design for deployment of MOX-fueled reactors, including under hypothetical accident conditions. Herein, we use aerodynamic levitation, laser beam heating, and X-ray total scattering to measure the structure of PuO_{2-x} up to 3000 ± 50 K under various oxygen partial pressures. We demonstrate, by analogous measurements on cerium oxides, that its melt is structurally similar to CeO_{2-x}, a commonly used nonradioactive surrogate for PuO_{2-x}.

For high-temperature structure measurements, high-energy synchrotron X-ray diffraction was performed with aerodynamically levitated and laser beam heated PuO_{2-x} spheroids ~2 mm in diameter[15]. The levitation technique enables high-temperature studies without risking sample contamination from container interactions. As shown in Fig. 1a, diffraction was measured by transmission of X-rays through the top of the sample, where the heating laser and an optical pyrometer were aligned. Samples initially appeared matte grey and after heating were shiny black (Fig. 1b). Samples were heated and melted under 1% O_2 (Ar balance), Ar, or 5% CO (Ar balance) gases to access different O/Pu ratios (Fig. 1c). The relationship between fluorite PuO_{2-x} (f-PuO_{2-x}) composition and oxygen partial pressure, previously determined from experimental data up to 2050 K[16], was extrapolated to the solidus and yielded melt compositions of $PuO_{1.76}$, $PuO_{1.69}$, and $PuO_{1.57}$ for the gases used here. For example, the heating trajectory for a sample

heated in 5% CO is shown in Fig. 1c with pink shading. (Compositional uncertainty in O/Pu is ca. ± 0.03, as discussed in the Supplementary Information (SI) along with a comparison of different published oxidation models.) Heating was attempted with pure O_2 gas, but PuO_{2-x} volatilized severely above 2300 K and full melting was not achieved (Fig. 1c, inset); further heating in O_2 was aborted to avoid rapid sample loss by volatilization. This raises considerations pertinent to accidental melting of MOX fuels, which upon contacting air may release vapors containing plutonium oxides.

X-ray diffraction data were reduced and corrected to obtain the total X-ray structure factor, *S(Q)*, where Q is the magnitude of the scattering vector, $Q = 4\pi \sin(\theta)/\lambda$, 2θ is the scattering angle, and λ is the X-ray wavelength[17]. Figure 2a shows the PuO_{2-x} structure factors during heating under 5% CO (Ar balance) at temperatures shown by the red markers in Fig. 1c. The sample was initially a mixture of *f*-PuO_{2-x}, cubic α-Pu_2O_3, and hexagonal β-Pu_2O_3 with a mean composition of $PuO_{1.81}$. Upon heating, it transformed entirely to *f*-PuO_{2-x} between 1350 and 1530 K, consistent with the phase diagram. Diffuse scattering appeared above 1930 K, and upon further heating the Bragg peak intensities decreased while diffuse scattering increased, until the sample became fully molten between 2630 and 2730 K. Over this wide temperature range (2140-2630 K), the scattering is consistent with a mixture of mostly liquid and a small amount of *f*-PuO_{2-x}, which results from temperature gradients in the sample due to the focused spot of the heating laser and stochastic sample motions during the melting process. Temperature gradients result in uncertainty for levitated solids of typically ± 150 K[18] until they are fully molten (see SI). Sample motion can occur for solids just prior and during partial melting, during which time the sample is not stably aligned with the heating laser and X-ray beam. In the context of Fig. 1c, the heating trajectory shaded in pink is thus the general pathway, though different regions of the

sample were at varying locations along the trajectory, resulting in the observed solid/liquid mixture. For these reasons, compositional and lattice parameter calculations over 2140-2630 K should be treated with caution, and as such these data markers are shaded half-full in Figs. 1c and 2b. (Once fully molten, levitation was stable, and temperature uncertainty is typically ± 50 K.) The point of full melting (above 2630 K) is ~200 K higher than T_m = 2410 K according to the phase diagram, but the thermal gradients in partially-solid samples make any critical comparison of T_m difficult.

Figure 2b shows the change in atomic number density during heating under 5% CO (Ar balance). The *f*-PuO_{2-x} phase's density decreased approximately linearly from 300 to 1800 K and then asymptotically approached 0.0592 atoms $Å^{-3}$ as temperature approached T_m = 2410 K. These density changes occurred due to thermal expansion of the lattice (Fig. 2b, black line, from dilatometry[19]) and decreasing O/Pu ratio, corresponding to chemical expansion of the lattice (Fig. 2b, colored open squares, from X-ray diffraction[5]). The sample compositions estimated from equilibrium with the gas (Fig. 2b, see colors of triangle markers) have O/Pu ratios 0.03-0.06 higher than those predicted by extrapolation of prior chemical expansion data. The pink shaded trajectory in Fig. 1c illustrates this compositional uncertainty, which lies within the gas pO_2 uncertainty. As shown in Fig. 1c, upon reaching the solidus at a composition of $PuO_{1.65}$, the material melts isothermally while following the oxygen isobar to a composition of $PuO_{1.57}$. The arrest in lattice expansion (and density) upon approaching T_m is consistent with previous observations at much lower temperature (1273 K) that incremental chemical expansion diminishes as O/Pu decreases and approaches 1.61[5]. This behavior is likely because the O vacancies responsible for chemical expansion reach a high concentration and associate into

clusters[20]. Upon melting, $PuO_{1.57}$ density decreases to 0.0559 atoms Å^{-3} (9.65 g cm^{-3}), ~6% less than molten UO_2 (0.0593 atoms Å^{-3})[21] and consistent with the lower O content in $PuO_{1.57}$.

Figure 3a provides the X-ray structure factor for molten $PuO_{1.76}$ at 3000 K. The first principal peak position, Q_1, decreases by 0.014 Å^{-1} as O/Pu increases from 1.57 to 1.76. This small Q_1 variation suggests minimal redox-induced differences in Pu-Pu periodicity and the Pu-O polyhedral units that comprise the melt structure. In contrast, molten UO_{2-x} composition varies much more than PuO_{2-x} over this pO_2 range[22]: O/U is likely less than 1 in 5% CO (Ar balance) and increases to 1.93 under Ar, but Q_1 increases only 0.03 Å^{-1}. This suggests that Q_1 is only weakly sensitive to redox-induced structural changes, and/or that cation-cation periodicity changes are subtle.

Figure 3b shows the X-ray weighted total pair distribution function (PDF), $T(r)$, for $PuO_{1.76}$, obtained from the sine Fourier transform of the structure factor[17]. The PDF's first peak is too broad and asymmetric to be fitted well with a single Gaussian distribution (Extended Data Fig. 1a). The necessity of fitting with two distinct Pu-O distributions motivated the use of separate Pu(III) and Pu(IV) species in an atomic structure model, created using empirical potential structure refinement (EPSR)[23]. The EPSR model agrees well with the X-ray scattering data (Fig. 3a-c). The model's atomic partial pair correlations (Fig. 3b) show overlapping Pu(III)-O and Pu(IV)-O distributions with mean bond lengths of 2.55 and 2.29 Å and mean coordination numbers of 6.0(5) and 5.8(5). The relatively shorter mean bond length for Pu(IV)-O is consistent with its larger charge, given the similar mean coordination numbers for both Pu(III)-O and Pu(IV)-O. The overall Pu-O mean coordination is 5.9(4), compared to $n_{PuO} = 8$ for f-PuO_2 and 6 for α-Pu_2O_3 (Fig. 3d). Using the average of the crystalline phases, since $PuO_{1.76}$ lies midway compositionally, the melt n_{PuO} is 5.9/7 = 84% of that in the crystal, which is similar to molten

UO_2: n_{UO} = 6.7, or 6.7/8 = 84% of the crystal[21]. The $PuO_{1.76}$ melt structure consists of Pu-O polyhedra with coordination ranging from 4 to 8, with preferential clustering of polyhedra with similar coordination (Fig. 3c). Polyhedra are connected by 65% corner-, 29% edge-, and 6% face-sharing.

A longstanding question in actinide chemistry is the extent to which 5*f* valence orbitals participate in covalent bonds[24]. If Pu-O bonding has different covalency than the lanthanides, this property could be exploited to improve chemical processing methods for used nuclear fuel that separate Pu from lanthanide fission products. Both solid and liquid UO_2 are mostly ionic, indicative of highly localized 5*f* electrons[21,25,26]. Density functional theory (DFT) calculations on the actinide dioxides ThO_2 through EsO_2 have revealed some covalency in the intermediate region of PuO_2 to CmO_2, evidenced by degeneracy between actinide 5*f* and O 2*p* orbitals beginning with PuO_2[26–28]. This trend in covalency has also been linked with the lower oxidation tendency of NpO_2 and PuO_2 compared to UO_2, which exhibits an energy gap between U 5*f* and O 2*p*[29]. However, X-ray absorption near edge structure and resonant inelastic X-ray scattering measurements on PuO_2 in solution have indicated that the 5*f* states in Pu are less active in the chemical bonding[30].

To investigate whether Pu-O covalency is present in the melts, another modeling approach was implemented since EPSR cannot provide information on electronic structure. A machine-learned Gaussian approximation potential[31] (GAP) was developed at the level of DFT+U calculations (including Coulomb potential) for PuO_{2-x} and then implemented in a molecular dynamics (MD) simulation[32]. (See SI for details.) In prior works, MD simulations based on empirical potentials have often been relied on for calculating properties such as density, enthalpy, specific heat, bulk modulus, and melting points[3,13,14] for compositionally complex phases in

nuclear fuels and under extreme conditions that are difficult to access experimentally. One major limitation is developing MD potentials that can reproduce experimental data, and most MD models are validated using only solid phase information due to the lack of liquid and high-temperature experiments. Empirical potentials also have the limitation of only treating one cation oxidation state, for example in prior MD modeling of molten UO_2[21].

The GAP-MD model here agrees well with the liquid structure X-ray measurement for $PuO_{1.76}$ (Fig. 3a-b), illustrating why such measurements are crucial to validating the structural models that are used to estimate material properties. The projected density of states (PDOS) was calculated from the model and is shown in Fig. 3e. Below the highest occupied state, the significant degeneracy between Pu 5*f* and O 2*p* orbitals suggest that some covalency is present in the melt structure. This finding of covalency could be an important property that sets Pu-O apart from the lanthanides. While similar to previous DFT+U results for crystalline PuO_2[26–28], this is the first such model for hypostoichiometric PuO_{2-x} compositions and for the liquid state. The GAP-MD approach is also an advancement in modeling the mixture of Pu(III) and Pu(IV) oxidation states, which is a challenge for empirical MD potentials.

Cerium oxide, CeO_{2-x} (Extended Data Fig. 2), is often used as a surrogate material for research on PuO_{2-x} to avoid radioactivity and toxicity hazards. Both Ce and Pu exist in 3+ and 4+ oxidation states, and their dioxides have similar redox activity and melting temperatures: CeO_2 at 3000 K (congruent, accessible only under high-pressure O_2)[33], and PuO_2 at 3017 K[12]. Surrogacy of CeO_{2-x} for PuO_{2-x} has been demonstrated for powder processing and sintering of MOX fuel pellets[34] and thermally induced gallium removal[35]. However, Ce(IV) is more easily reduced to Ce(III) as compared with Pu, which has made it an inadequate analogue for studies of Pu solubility in vitrified nuclear waste[36,37], chemical separation and purification processes including

PUREX and other aqueous technologies[38], and inorganic chemical synthesis[39]. In these cases, poor surrogacy arises from the larger Ce(III)/Ce(IV) ratio compared to Pu(III)/Pu(IV) for certain ranges of oxygen potential, though under highly oxidizing conditions the surrogacy is improved[40]. This motivates an evaluation of Ce surrogacy for Pu in the oxide melts.

Figure 4a shows the PDFs for $PuO_{1.76}$, melted under 1% O_2 (Ar balance) at 3000 K, and $CeO_{1.75}$, melted under pure O_2 at 2580 K. The PDFs are qualitatively similar, though the relative peak magnitudes naturally differ due to the materials' different X-ray weighting factors (Extended Data: Fig. 3 and Table 1), arising from the different numbers of core electrons on the two cations. With the weighting factors removed, the atomic partial pair correlations for metal-oxygen (MO), metal-metal (MM), and oxygen-oxygen (OO) are nearly identical for the two EPSR models. The Ce-O first coordination shell is slightly broader than Pu-O, though with similar mean coordination (6.1(4) vs. 5.9(4)). The distributions of M-O and O-M coordination environments are also similar (Fig. 4b-c). M-O coordination has a mode of 6 and approximately equal portions of MO_5 and MO_7. The M(III)-O pairs are slightly shifted to less 5-coordinate and more 7-coordinate, as compared to M(IV)-O pairs. The O-M coordination is mostly 3- and 4-coordinate with a variety of O-{M(III),M(IV)} local environments. Higher O-M coordination correlates with environments richer in M(III).

Bond angle distributions for O-M-O and M-O-M are nearly identical for $PuO_{1.76}$ and $CeO_{1.75}$ melts (Fig. 4d), both showing broad distributions indicative of distorted polyhedra with varying coordination. The O-M-O peaks near 80 and 170° likely represent the octahedral MO_6 species, which are more similar to the α-Pu_2O_3 crystalline phase than *f*-PuO_2. Statistics for shortest-path -M-O- rings[41] are also similar in the two melts (Fig. 4e). Modal ring size is 4 cations. Only 17% of atoms participate in rings with 5 cations, and almost no rings contain more than 5 cations.

This lack of larger rings matches other non-glass-forming oxide melts, such as HfO_2[42], in contrast to glass-forming systems like SiO_2 that contain substantial populations of 6- and 7-cation rings[41].

The similarity in X-ray PDFs and structural models for $PuO_{1.76}$ and $CeO_{1.75}$ indicate that cerium oxide is an excellent liquid structure analogue for plutonium oxide, once differences in redox activity are adjusted to obtain similar M(III)/M(IV) ratios. This suggests that Ce surrogacy for Pu could be improved in other applications such as nuclear waste vitrification, if oxidation potential differences can be judiciously corrected. The structural similarity of the melts is also consistent with their bonding character: like PuO_{2-x}, DFT calculations and X-ray absorption spectroscopy for crystalline *f*-CeO_2 have evidenced some covalent character via degeneracy of Ce 4*f* and O 2*p* orbitals[43].

Atomistic structural knowledge of molten plutonium oxide and its redox dependence provide useful experimental data to validate structural and thermochemical modeling for Pu-O, Pu-U-O, and other MOX fuels in the high-temperature range encompassing their melting points. Such modeling efforts remain a primary route for estimating thermophysical properties and material behavior in extreme operating conditions, which are necessary for engineering and safety design of advanced nuclear power reactors.

Online content

Any methods, additional references, Nature Portfolio reporting summaries, source data, extended data, supplementary information, acknowledgements, peer review information; details of author contributions and competing interests; and statements of data and code availability are available at [URL].

1. Abram, T. & Ion, S. Generation-IV nuclear power: A review of the state of the science. *Energy Policy* **36**, 4323–4330 (2008).
2. Fouquet-Métivier, P. *et al.* Investigation of the solid/liquid phase transitions in the U–Pu–O system. *Calphad* **80**, 102523 (2023).
3. Guéneau, C., Chartier, A., Fossati, P., Van Brutzel, L. & Martin, P. Thermodynamic and Thermophysical Properties of the Actinide Oxides. in *Comprehensive Nuclear Materials 2nd edition* 111–154 (Elsevier, 2020). doi:10.1016/B978-0-12-803581-8.11786-2.
4. Tokar, M., Nutt, A. W. & Keenan, T. K. Linear Thermal Expansion of Plutonium Dioxide. *Nucl. Technol.* **17**, 147–152 (1973).
5. Gardner, E. R., Markin, T. L. & Street, R. S. The plutonium-oxygen phase diagram. *J. Inorg. Nucl. Chem.* **27**, 541–551 (1965).
6. Intergovenmental Panel on Climate Change. *Climate Change 2022: Mitigation of Climate Change* (2022).
7. Chang, Y. Il *et al.* Conceptual Design of a Pilot-Scale Pyroprocessing Facility. *Nucl. Technol.* **205**, 708–726 (2019).
8. Carbajo, J. J., Yoder, G. L., Popov, S. G. & Ivanov, V. K. A review of the thermophysical properties of MOX and UO2 fuels. *J. Nucl. Mater.* **299**, 181–198 (2001).
9. IAEA. *Status and Advances in MOX Fuel Technology*. (2003).
10. Vauchy, R., Joly, A. & Valot, C. Lattice thermal expansion of Pu1−yAmyO2-x plutonium–americium mixed oxides. *J. Appl. Crystallogr.* **50**, 1782–1790 (2017).
11. Boivineau, J. C. Etude par rayons x du diagramme plutonium-oxygene de la temperature ambiante jusqu'a 1100°c. *J. Nucl. Mater.* **60**, 31–38 (1976).

12. De Bruycker, F. *et al.* Reassessing the melting temperature of PuO2. *Mater. Today* **13**, 52–55 (2010).

13. Ghosh, P. S. *et al.* Melting behavior of (Th,U)O2 and (Th,Pu)O2 mixed oxides. *J. Nucl. Mater.* **479**, 112–122 (2016).

14. Cooper, M. W. D., Murphy, S. T., Rushton, M. J. D. & Grimes, R. W. Thermophysical properties and oxygen transport in the (Ux,Pu1-x)O2 lattice. *J. Nucl. Mater.* **461**, 206–214 (2015).

15. Weber, J. K. R. *et al.* Aerodynamic levitator for in situ x-ray structure measurements on high temperature and molten nuclear fuel materials. *Rev. Sci. Instrum.* **87**, 073902 (2016).

16. Besmann, T. M. & Lindemer, T. B. Chemical thermodynamic representations of <PuO2-x> and <U1-zPuzOw>. *J. Nucl. Mater.* **130**, 489–504 (1985).

17. Benmore, C. J. X-Ray Diffraction from Glass. in *Modern Glass Characterization* 241–270 (John Wiley & Sons, Inc., 2015).

18. McCormack, S. J., Tamalonis, A., Weber, R. J. K. & Kriven, W. M. Temperature gradients for thermophysical and thermochemical property measurements to 3000 °C for an aerodynamically levitated spheroid. *Rev. Sci. Instrum.* **90**, 15109 (2019).

19. Uchida, T., Sunaoshi, T., Konashi, K. & Kato, M. Thermal expansion of PuO2. *J. Nucl. Mater.* **452**, 281–284 (2014).

20. Kato, M., Nakamura, H., Watanabe, M., Matsumoto, T. & Machida, M. Defect chemistry and basic properties of non-stoichiometric PuO2. *Defect Diffus. Forum* **375**, 57–70 (2017).

21. Skinner, L. B. *et al.* Molten uranium dioxide structure and dynamics. *Science* **346**, 984–987 (2014).

22. Alderman, O. L. G. *et al.* The structure of liquid UO2−x in reducing gas atmospheres. *Appl. Phys. Lett.* **110**, 081904 (2017).

23. Soper, A. K. Empirical potential Monte Carlo simulation of fluid structure. *Chem. Phys.* **202**, 295–306 (1996).

24. Neidig, M. L., Clark, D. L. & Martin, R. L. Covalency in f-element complexes. *Coord. Chem. Rev.* **257**, 394–406 (2013).

25. Desgranges, L., Baldinozzi, G., Fischer, H. E. & Lander, G. H. Temperature-dependent anisotropy in the bond lengths of UO2 as a result of phonon-induced atomic correlations. *J. Phys. Condens. Matter* **35**, 10LT01 (2023).

26. Wen, X. D., Martin, R. L., Henderson, T. M. & Scuseria, G. E. Density functional theory studies of the electronic structure of solid state actinide oxides. *Chem. Rev.* **113**, 1063–1096 (2013).

27. Prodan, I. D., Scuseria, G. E. & Martin, R. L. Covalency in the actinide dioxides: Systematic study of the electronic properties using screened hybrid density functional theory. *Phys. Rev. B* **76**, 033101 (2007).

28. Yang, Y. & Zhang, P. Chemical bonds and vibrational properties of ordered (U, Np, Pu) mixed oxides. *J. Appl. Phys.* **113**, 013501 (2013).

29. Andersson, D. A., Lezama, J., Uberuaga, B. P., Deo, C. & Conradson, S. D. Cooperativity among defect sites in AO2+x and A4O9 (A=U,Np,Pu): Density functional calculations. *Phys. Rev. B* **79**, 024110 (2009).

30. Vitova, T. *et al.* The role of the 5f valence orbitals of early actinides in chemical bonding. *Nat. Commun.* **8**, 16053 (2017).

31. Bartók, A. P., Payne, M. C., Kondor, R. & Csányi, G. Gaussian Approximation Potentials:

The Accuracy of Quantum Mechanics, without the Electrons. *Phys. Rev. Lett.* **104**, 136403 (2010).

32. Sivaraman, G. *et al.* Experimentally Driven Automated Machine-Learned Interatomic Potential for a Refractory Oxide. *Phys. Rev. Lett.* **126**, 156002 (2021).

33. Zinkevich, M., Djurovic, D. & Aldinger, F. Thermodynamic modelling of the cerium-oxygen system. *Solid State Ionics* **177**, 989–1001 (2006).

34. Kim, H. S. *et al.* Applicability of CeO2 as a surrogate for PuO2 in a MOX fuel development. *J. Nucl. Mater.* **378**, 98–104 (2008).

35. Kolman, D. G., Park, Y., Stan, M., Hanrahan, R. J. & Butt, D. P. An assessment of the validity of cerium oxide as a surrogate for plutonium oxide gallium removal studies. *LA-UR-99-0491* (1999).

36. Darab, J. G. *et al.* Redox chemistry of plutonium and plutonium surrogates in vitrified nuclear wastes. *J. Am. Ceram. Soc.* **105**, 6627–6639 (2022).

37. Cachia, J. N. *et al.* Enhancing cerium and plutonium solubility by reduction in borosilicate glass. *J. Nucl. Mater.* **352**, 182–189 (2006).

38. Feuchter, H. *et al.* Influence of light and temperature on the extractability of cerium(IV) as a surrogate of plutonium(IV) and its effect on the simulation of an accidental fire in the PUREX process. *ACS Omega* **4**, 12896–12904 (2019).

39. Lin, J., Cross, J. N., Diwu, J., Meredith, N. A. & Albrecht-Schmitt, T. E. Comparisons of plutonium, thorium, and cerium tellurite sulfates. *Inorg. Chem.* **52**, 4277–4281 (2013).

40. Zamoryanskaya, M. V & Burakov, B. E. Feasibility Limits in Using Cerium as a Surrogate for Plutonium Incorporation in Zircon, Zirconia and Pyrochlore. *MRS Online Proc. Libr.* **663**, 301 (2000).

41. Le Roux, S. & Jund, P. Ring statistics analysis of topological networks: New approach and application to amorphous GeS2 and SiO2 systems. *Comput. Mater. Sci.* **49**, 70–83 (2010).
42. Sivaraman, G. *et al.* A Combined Machine Learning and High-Energy X-ray Diffraction Approach to Understanding Liquid and Amorphous Metal Oxides. *J. Phys. Soc. Japan* **91**, 091009 (2022).
43. Minasian, S. G. *et al.* Quantitative Evidence for Lanthanide-Oxygen Orbital Mixing in CeO2, PrO2, and TbO2. *J. Am. Chem. Soc.* **139**, 18052–18064 (2017).
44. Guéneau, C. *et al.* Thermodynamic modelling of advanced oxide and carbide nuclear fuels: Description of the U-Pu-O-C systems. *J. Nucl. Mater.* **419**, 145–167 (2011).

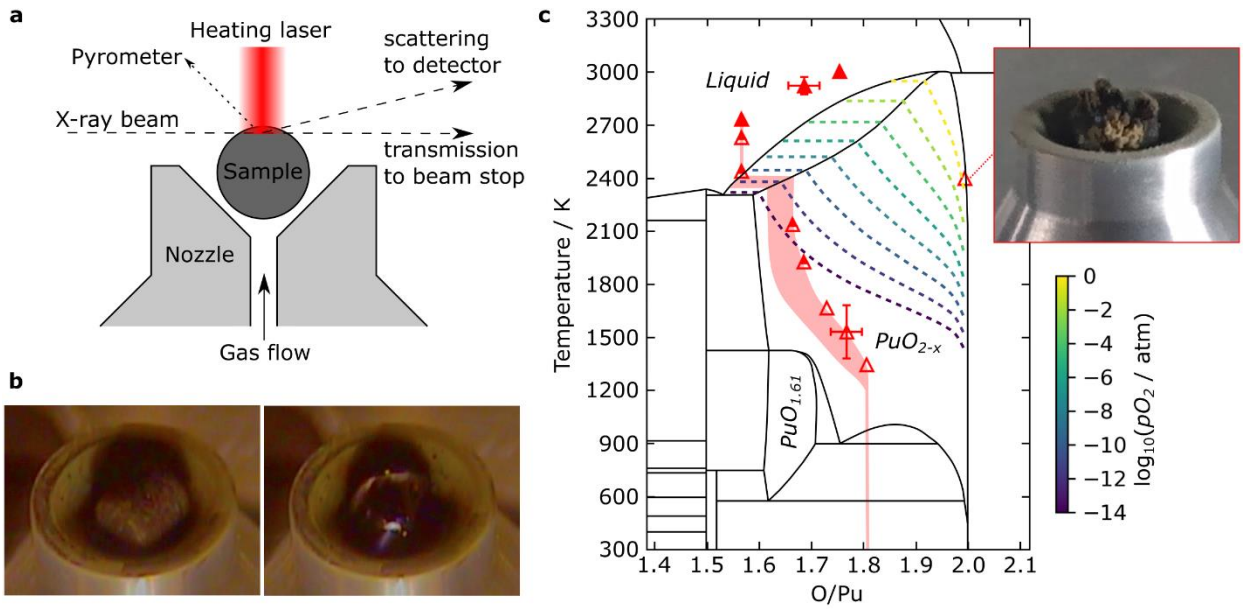

Fig. 1. Aerodynamic levitation and laser beam heating of PuO_{2-x} high-temperature solids and melts. a, Cross-section schematic of the sample on the levitation nozzle. **b,** Pictures of a PuO_{2-x} pellet before (left) and after (right) melting under 5% CO (Ar balance). **c,** Pu-O phase diagram[44] with oxygen gas partial pressure (pO_2) isobars (dashed colored curves)[16]. X-ray scattering measurements were taken at the red triangle markers (no fill = solid; filled = liquid; half-filled = solid/liquid mixture). The redox trajectory for a sample heated in 5% CO (Ar balance) is shaded in pink. Representative error bars are shown for solid and liquid measurements. The inset picture is a sample after heating under pure O_2 gas, which exhibited severe volatilization before reaching T_m.

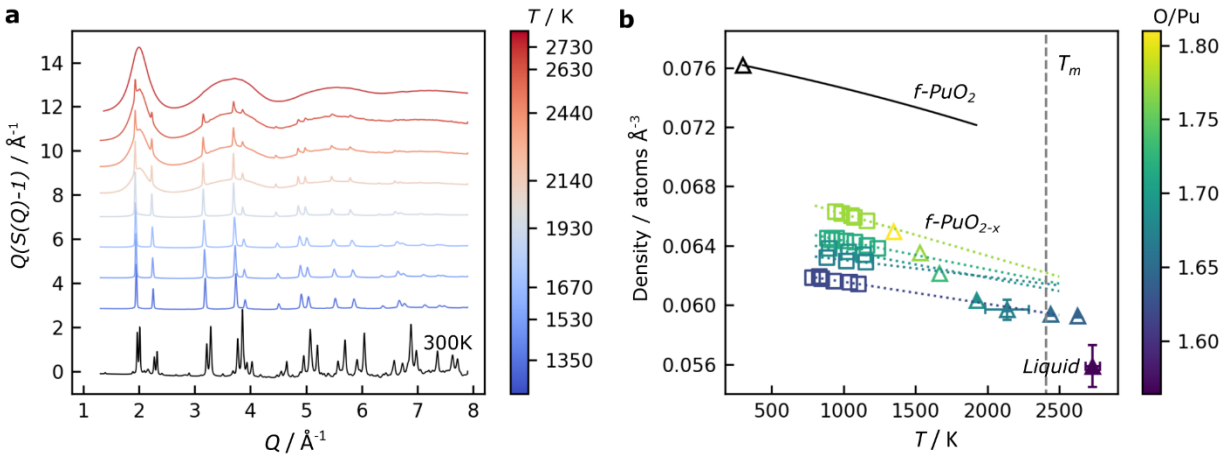

345

346 **Fig. 2. X-ray total scattering of high-temperature PuO_{2-x}. a,** X-ray structure factors under 5%

347 CO (Ar balance). **b,** Atomic number density measured for *f*-PuO_{2-x} and liquid (triangles), with

348 markers' colors corresponding to the O/Pu ratio given by the pO_2 isobars in Fig. 1c. Triangle

349 markers are unfilled for solid samples, filled for liquid samples, and half-filled for solid/liquid

350 mixtures. Representative error bars are shown for solid and liquid measurements. Density

351 changes due to thermal expansion (black line)[19] and chemical reduction (colored squares)[5] are

352 shown up to the maximum temperatures previously reported.

353

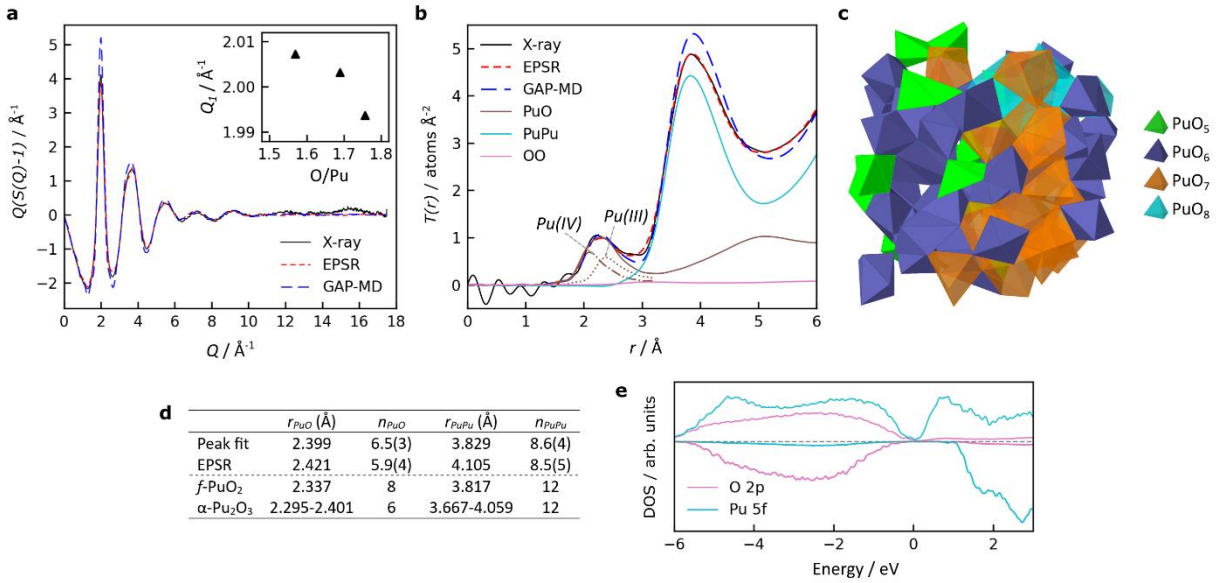

	r_{PuO} (Å)	n_{PuO}	r_{PuPu} (Å)	n_{PuPu}
Peak fit	2.399	6.5(3)	3.829	8.6(4)
EPSR	2.421	5.9(4)	4.105	8.5(5)
f-PuO_2	2.337	8	3.817	12
α-Pu_2O_3	2.295-2.401	6	3.667-4.059	12

Fig. 3. Structure of molten $PuO_{1.76}$. a, X-ray structure factor and comparison to models from empirical potential structure refinement (EPSR) and Gaussian approximation potential[31] driven molecular dynamics (GAP-MD). Inset: position of the first principal peak for liquids of differing compositions. **b,** Total pair distribution function (PDF) with comparison to models and the EPSR X-ray weighted atomic partial pair correlations (Q_{max} = 17.4 Å^{-1}). The Pu-O partial comprises separate contributions for Pu(III)-O and Pu(IV)-O, shown with dashed lines up to their cutoff distance used for structure calculations (r = 3.21 Å, corresponding to the minimum in the total Pu-O partial). **c,** Atomic structure snapshot from the EPSR model. **d,** Mean bond distances and coordination numbers obtained from Gaussian peak fitting and EPSR, compared with the crystal phases. **e,** Averaged projected density of states (DOS) for Pu 5*f* and O 2*p* electrons. The highest occupied state is set to zero, and spin-up and spin-down components are displayed as positive and negative values.

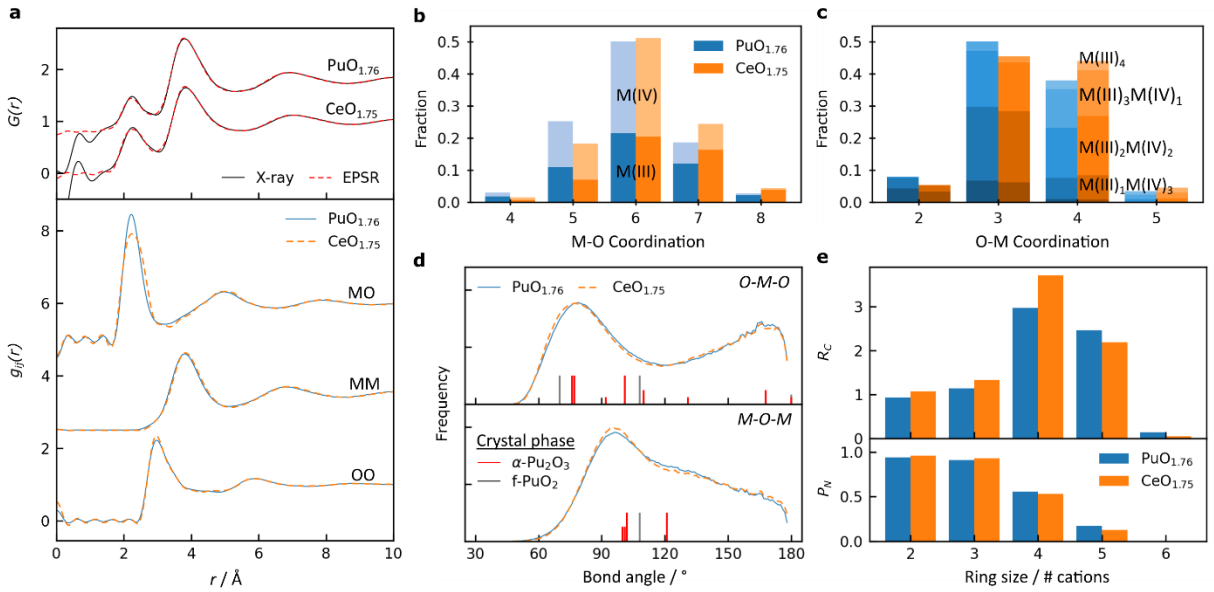

Fig. 4. Structural surrogacy of CeO_{2-x} for PuO_{2-x} melts. a, X-ray weighted PDFs, *G(r)*, for $PuO_{1.76}$ at 3000 K and $CeO_{1.75}$ at 2580 K, compared with their EPSR models (Q_{max} = 11.9 Å^{-1}). Unweighted atomic partial pair PDFs, $g_{ij}(r)$, from EPSR for metal-oxygen (MO), metal-metal (MM), and oxygen-oxygen (OO) pairs in the two melts. **b,** Distribution of M-O coordination numbers, separated by oxidation state into M(III)-O and M(IV)-O components. **c,** Distribution of O-M coordination numbers. Increasing darkness of the color bars represents O local environments with increasing number of M(IV) neighbors. **d,** Distributions for O-M-O and M-O-M bond angles, after division by the *sin(θ)* dependence for a random angle distribution, compared with the crystalline phases for *f*-PuO_2 and α-Pu_2O_3. **e,** Frequency of shortest-path -M-O- rings, R_C, and the fraction of atoms participating in rings of a given size, P_N. Fractions do not sum to unity since a given atom can participate in multiple rings.

Methods

Sample preparation and containment

Three PuO_{2-x} pellets were prepared by uniaxially pressing PuO_2 powder (>99% chemical purity) with stearic acid as a binder in a stainless steel die. Powder isotopically enriched with ^{242}Pu (>99.9% radionuclidic purity) was used to minimize radioactivity safety risks. The pressed pellets were heated at 280 K min^{-1} to bake out the binder and sintered at 1920 K for 1 h under vacuum in a Mo-lined graphite crucible, followed by air milling to round off the corners of the cylindrical pellets. The resulting samples were spheroid in shape with a diameter of ~2.5 mm, each 78-82 mg. Rietveld refinement of one pellet's X-ray diffraction pattern indicated a mixture of *f*-PuO_{2-x}, cubic α-Pu_2O_3, and hexagonal β-Pu_2O_3 with a mean composition of $PuO_{1.81}$, which is close to the composition $PuO_{1.82}$ previously identified for congruent evaporation[45]. Three samples were then loaded into a radioactive containment vessel inside a hermetically sealed chamber designed for aerodynamic levitation of nuclear fuel materials[15]. The sample containment vessel resided in an antechamber to the main chamber, which contained the levitation nozzle and several ports for laser, camera, pyrometer, and X-ray access and egress (see SI for further details on instrumentation and radiological safety procedures). The containment vessel also included two beads of NIST-standard CeO_2 mounted in epoxy, used for calibration of the sample-detector distance during X-ray measurements, and two ZrO_2 beads that were used for precise alignment of the levitation position, laser heating beam, and X-ray beam.

CeO_2 spheroids, ~2 mm in diameter and 70-80 mg, were prepared by melting CeO_2 powder (99.9%, Aldrich) in a copper hearth with a 10.6 μm laser.

405 **X-ray total scattering**

406 The aerodynamic levitator and chamber containing the samples were installed at Sector 6-ID-
407 D of the Advanced Photon Source, Argonne National Laboratory (Argonne, IL, USA). A vacuum
408 chuck integrated with the chamber was used to transfer samples between the containment vessel
409 and the adjoining levitation chamber. The sample levitation position was aligned with the
410 incoming X-ray beam, a video camera, and an optical pyrometer (λ = 0.9 μm, 975-3775 K,
411 Chino) for temperature measurements. Sample emissivity was assumed to be 0.92 for pyrometer
412 temperature correction, based on prior studies on molten oxides[46] (see SI). Diffraction of
413 transmitted 99.959 keV X-rays passing through the top of the spheroid sample was measured
414 with an area detector (Varex 4343CT), which was covered with a 1 mm thick brass sheet to
415 preferentially attenuate Pu L-edge fluorescence near 23 keV. The X-ray beam at the sample
416 position was 0.2 mm tall and 0.5 mm wide. Background diffraction measurements taken without
417 a sample were used to subtract the scattering contributions from 1 mm thick silica windows on
418 the chamber and the gas along the X-ray path. A small tungsten beam stop was placed
419 immediately downstream of the silica exit window to further minimize its scattering, which
420 blocked X-rays at scattering vectors below Q_{min} = 1.3 Å^{-1}. The detector was positioned at a
421 distance from the sample of either 1320 or 420 mm. The longer distance provides better Q
422 resolution for Bragg peaks, while the shorter distance achieves a larger Q range (up to 23.3 Å^{-1})
423 necessary for high resolution PDF analysis. For a given sample, heating and measurements of the
424 solid were collected first using the 1320 mm detector distance. Then the sample was cooled and
425 the detector was repositioned to 420 mm, followed by heating and liquid measurements.

426 Samples were levitated using a gas stream of either O_2, 1% O_2 (Ar balance), ultrahigh purity
427 Ar, or 5% CO (Ar balance), and heated with a 10.6 μm laser (Synrad i401, spot diameter ~1mm

at sample position)[47]. Heating was increased incrementally, alternating with diffraction measurements of the sample held isothermally at temperatures ranging 1350-3000 K (Extended Data Fig. 4a). Measurements were not taken for heated samples below 1350 K due to reduced temperature stability in the lower range of laser power. The uncertainty in sample temperatures is estimated as ± 150 K for solids and ± 50 K for liquids (see SI).

X-ray diffraction measurements of CeO_{2-x} samples were collected in a similar setup, without the nuclear materials chamber.

Data analysis

The area detector distance and tilt were calibrated with Fit2D[48] using diffraction patterns of NIST-standard CeO_2. Sample diffraction patterns were then azimuthally integrated in Fit2D and corrected for flat field, X-ray polarization, oblique incidence and detector attenuation effects[49]. Background subtraction, sample attenuation and multiple scattering corrections, and subtraction of self and Compton scattering were performed using GudrunX[50] to obtain the normalized total X-ray structure factors, *S(Q)*[17]. The structure factor is a summation of the atomic partial pair structure factors, $s_{ij}(Q)$, for atom types i and j. These partials are weighted by the normalized Faber-Ziman weighting factors[51], $W_{ij}(Q)$:

$$S(Q) = \sum_{i,j \geq i} W_{ij}(Q) s_{ij}(Q) \quad (1)$$

$$W_{ij}(Q) = \frac{(2 - \delta_{ij}) c_i c_j f_i(Q) f_j(Q)}{\langle f(Q) \rangle^2} \quad (2)$$

where c_i are the fractional atomic concentrations and $f_i(Q)$ are the X-ray free-atom atomic form factors[52]. Weighting factors for all molten samples are given in Extended Data Table 1, for $Q = 0$ Å^{-1}, and plotted as functions of Q in Extended Data Fig. 3.

For measurements of solid samples, Rietveld refinements for crystalline phases were performed in GSAS-II[53] (Extended Data Fig. 5). X-ray diffraction patterns were compared against fluorite PuO_2 (*f*-PuO_2), α-Pu_2O_3, β-Pu_2O_3, PuO, and all phases of metallic Pu (α, β, γ, δ, δ', and ε). Instrument parameters were refined using NIST-standard CeO_2 and not modified during sample pattern refinement. Sample parameters were refined iteratively. First, the background was fitted. Next, the scaling factor and lattice parameter were refined, followed by crystallite size. These steps were followed first for the predominant phase *f*-PuO_{2-x} and then repeated for the minority phases. For the PuO_{2-x} phase, texture (preferred orientation) was also refined to improve the goodness-of-fit. Texture refinement is justified due to two known limitations of the levitation method for crystal X-ray diffraction: (i) quenching of levitated melts often results in a sample containing only a few crystallites of very large size, and (ii) the gas flow provides inconsistent rotation of the sample, so the diffraction pattern obtained is not a proper orientational average. The data resolution was insufficient to draw quantitative insights on crystallite size or texture, but the goal of refining these parameters was to improve accuracy of the lattice parameter and phase fraction determinations. For the initial material and recovered samples, mean compositions were calculated based on the phase fractions determined from Rietveld refinements.

For liquid measurements, the low-*Q* range of *S(Q)* below 1.4-1.5 $Å^{-1}$ was extrapolated by fitting a Lorentzian distribution to the first principal peak (Extended Data Fig. 6), while constraining the fit to match the theoretical value for *S(0)*[54], assuming isothermal compressibility is zero for the liquids. The "top hat" convolution[55] in GudrunX was used to reduce long-wavelength background in *S(Q)* that otherwise manifests as oscillations in the nonphysical region

of the PDFs at $r < 1$ Å (Extended Data Fig. 7). Then, the PDFs were obtained by the Fourier transform:

$$G(r) = 1 + \frac{1}{2\pi^2 \rho r} \int_0^{Q_{max}} Q(S(Q) - 1) \sin(Qr)\, dQ \quad (3)$$

$$T(r) = 4\pi\rho r G(r) \quad (4)$$

For PuO_{2-x}, based on the signal-to-noise present in *S(Q)*, a Q_{max} of 17.4 Å^{-1} was selected. Sample density, ρ, ranged 0.0559-0.0572 atoms Å^{-1} (9.28-9.65 g cm^{-3}) depending on sample composition. For $CeO_{1.75}$, ρ = 0.0575 atoms Å^{-1} (5.84 g cm^{-3}) and Q_{max} = 11.9 Å^{-1}. These density values were estimated from the low-*r* slope in *T(r)* and are within 5% of estimates based on literature data for the high-temperature crystals and anticipated volume changes upon melting. (See SI for further discussion.)

Sample compositions in the *f*-PuO_{2-x} phase were calculated using the relationship with gas pO_2[16] (see SI for discussion of composition calculations and uncertainty). For *f*-CeO_{2-x}, the composition-pO_2 relationship was extrapolated from experimental data[33]. Because oxygen activity is not known for the liquids, the liquid compositions were assigned the values present at the liquidi.

NXFit[56] was used to fit Gaussian distributions, convolved with the correct peak-shape functions, to the total PDFs, from which mean bond distances and coordination numbers were extracted (Extended Data Fig. 1).

Empirical potential structure refinement

Structural models for molten $PuO_{1.76}$ and $CeO_{1.75}$ were obtained using EPSR[23,57]. The EPSR technique begins by defining a simulation volume of specified composition, density, and temperature. Atomic positions are initially equilibrated using Lennard-Jones and pseudo-

Coulomb potentials, after which the X-ray scattering data are introduced in a reverse Monte Carlo simulation that refines the interatomic potentials to bring the model toward agreement with experimental scattering data (the so-called "empirical potential"). Each model was initialized with a mixture of 3+ and 4+ oxidation states for the cations, with the atomic concentrations set to match the compositions. A simulation box containing 1596 atoms (ρ = 0.0571 atoms Å^{-3} for $PuO_{1.76}$ or 0.0575 atoms Å^{-3} for $CeO_{1.75}$, edge length ~30.3 Å) was equilibrated using the pairwise potentials given in Table S1 in the SI. For O^{2-}, the potential parameters were taken from prior EPSR models for metal oxide liquids[58,59] and adjusted slightly to improve agreement between the equilibrated model (without empirical potential) and the X-ray scattering data. For Pu(III) and Pu(IV), the Lennard-Jones atomic radii (σ) were chosen so that the cation-oxygen pairs had bond distances that matched those obtained from Gaussian peak fitting of the PDFs (Extended Data Fig. 1), again with slight adjustments to improve the equilibrated model. Values were explored for the cations' ε parameters ranging 1.0-2.3, but the final model (after empirical potential) was not significantly influenced. The chosen values (1.5 kJ mol^{-1}) are within the range of cations used in other oxide liquid models[59]. For consistency, the same reference potentials were applied for Ce(III) and Ce(IV) as for Pu(III) and Pu(IV).

After at least 10,000 step iterations to equilibrate the models at 3000 K, the X-ray structure factors were introduced to drive refinement of the so-called "empirical potential" with EPSR's reverse Monte Carlo approach, which improves the model's agreement with the X-ray data. The scattering data were introduced as an empirical potential and applied at a magnitude of 10-20% of the system energy. After at least 10,000 iterations, the structure factor of the model was calculated and averaged over an additional 7,500 iterations.

To analyze the short- and intermediate-range atomic order, a cutoff distance of 3.21 Å was used for Pu-O and Ce-O, corresponding to the minima in the atomic partial pair correlation after its first peak. Connectivity between Pu-O or Ce-O polyhedra was assessed by counting the number of O shared between neighboring cations. Bond angle distributions, coordination number distributions, and ring statistics[41] according to King's criterion[60] were calculated using Atomes[61]. Bond angle distributions are normalized by the *sin(θ)* dependence that would occur for a random distribution.

Sensitivity of the model to initial reference potentials, temperature, and composition is discussed in the SI.

Density functional theory

Spin polarized DFT calculations were performed with the plane-wave Vienna *ab initio* simulation package (VASP) using projected augmented wave (PAW) pseudo-potentials[62,63]. The exchange correlation term was modelled using the generalized gradient approximation (GGA) of Perdew, Burke and Ernzeroff (PBE)[64]. A plane wave cutoff of 650 eV was found to be suitable[65], and an electronic convergence criterion of 10^{-6} eV was used. A Γ-centered 1×1×1 k mesh was used for reciprocal sampling. To accurately describe the behavior of the localized Pu 5*f* states, the orbital-dependent Coulomb potential (U) and exchange parameter (J) were applied within the rotationally invariant DFT+U formalism of Liechtenstein *et al.*[66], with U = 4.5 eV and J = 0.5 eV[67,68]. A Grimme "D3" dispersion correction was included[69,70].

Gaussian approximation potential and molecular dynamics

A machine-learned Gaussian approximation potential[31] (GAP) was developed using two-body squared-exponential and many-body smooth overlap of atomic positions (SOAP) kernel functions[71,72] to measure chemical similarity between local chemical neighborhoods. To create a diverse training database, we utilized a previously developed active learning framework that can generate ultrafast sampling on small unit cells (i.e., 10s to 100s of atoms) using empirical force fields, followed by single point DFT+U[32,73,74]. The procedure was further iterated on generations of GAP models, leading to sufficient coverage of the training database[75,76].

To begin training, 75-atom unit cells of PuO_2 were melted with the available empirical force fields[14,77,78], starting with either (i) randomly packed atoms generated using packmol, or (ii) crystalline *f*-PuO_2. The structures were thermalized at 5000 K to ensure full melting, equilibrated to 3600 K, and then active learning was applied to ~15 ps trajectories sampled at 3600 K. To improve the diversity of the training database, samples were also drawn from *f*-PuO_2 at 300, 500, 1500, and 3000 K. DFT+U single point calculations were performed, and an initial GAP model was generated. With this model, liquid structures for the experimentally measured compositions ($PuO_{1.76}$, $PuO_{1.69}$, and $PuO_{1.57}$) were then sampled, starting from packmol generated inputs, followed by single point DFT+U and iterative retraining. Details of the final training database and GAP hyperparameters are summarized in Tables S2 and S3 of the SI, respectively. The GAP model validated on 52 independent test samples showed a root mean square error in energy and force of 7.68 meV $atom^{-1}$ and 0.45 eV $Å^{-1}$, respectively.

The GAP model was used to perform MD simulations of $PuO_{1.76}$ with a system size of 2,160 atoms at the same density as the experimental measurement, 0.0571 atoms $Å^{-3}$ (simulation box edge length of 33.57 Å). MD was performed using the LAMMPS software package compiled with the QUIP pair style[79,80]. The system was initially thermalized at 3600 K in the NVT

ensemble[81,82] and equilibrated at 3000 K. The NVT simulation was continued at 3000 K for 1.1 ns with a timestep of 0.5 fs, and the last 1 ns was used for structure calculations.

For PDOS calculations from the GAP-MD model, a smaller simulation box containing 80 atoms was used to aid convergence of the DFT+U calculations. More than 30 liquid structures at 3000 K were sampled with this approach, and the PDOS was averaged across this set of configurations.

Data availability

X-ray structure factor data for the $PuO_{1.76}$ and $CeO_{1.75}$ melts are provided in the Supplementary Information. All other relevant data are available from the corresponding author upon reasonable request.

45. Messier, D. R. Evaporation of Hypostoichiometric Plutonium Dioxide from 2070° to 2380°K. *J. Am. Ceram. Soc.* **51**, 710–713 (1968).

46. Krishnan, S., Weber, J. K. R., Schiffman, R. A., Nordine, P. C. & Reed, R. A. Refractive Index of Liquid Aluminum Oxide at 0.6328 μm. *J. Am. Ceram. Soc.* **74**, 881–883 (1991).

47. Weber, J. K. R., Benmore, C. J., Jennings, G., Wilding, M. C. & Parise, J. B. Instrumentation for fast in-situ X-ray structure measurements on non-equilibrium liquids. *Nucl. Instruments Methods Phys. Res. A* **624**, 728–730 (2010).

48. Hammersley, A. P. FIT2D: a multi-purpose data reduction, analysis and visualization program. *J. Appl. Crystallogr.* **49**, 646–652 (2016).

49. Skinner, L. B., Benmore, C. J. & Parise, J. B. Area detector corrections for high quality synchrotron X-ray structure factor measurements. *Nucl. Instruments Methods Phys. Res. A*

662, 61–70 (2012).

50. Soper, A. K. & Barney, E. R. Extracting the pair distribution function from white-beam X-ray total scattering data. *J. Appl. Crystallogr.* **44**, 714–726 (2011).

51. Faber, T. E. & Ziman, J. M. A theory of the electrical properties of liquid metals. *Philos. Mag. A J. Theor. Exp. Appl. Phys.* **11**, 153–173 (1965).

52. Waasmaier, D. & Kirfel, A. New analytical scattering-factor functions for free atoms and ions. *Acta Crystallogr.* **A51**, 416–431 (1995).

53. Toby, B. H. & Von Dreele, R. B. GSAS-II: the genesis of a modern open-source all purpose crystallography software package. *J. Appl. Crystallogr.* **46**, 544–549 (2013).

54. Skinner, L. B. *et al.* A time resolved high energy X-ray diffraction study of cooling liquid SiO2. *Phys. Chem. Chem. Phys.* **15**, 8566–8572 (2013).

55. Soper, A. K. Inelasticity corrections for time-of-flight and fixed wavelength neutron diffraction experiments. *Mol. Phys.* **107**, 1667–1684 (2009).

56. Pickup, D., Moss, R. & Newport, R. NXFit: A program for simultaneously fitting X-ray and neutron diffraction pair-distribution functions to provide optimized structural parameters. *J. Appl. Crystallogr.* **47**, 1790–1796 (2014).

57. Wilke, S. K., Alderman, O. L. G., Benmore, C. J., Neuefeind, J. & Weber, R. Octahedral oxide glass network in ambient pressure neodymium titanate. *Sci. Rep.* **12**, 8258 (2022).

58. Alderman, O. L. G., Skinner, L. B., Benmore, C. J., Tamalonis, A. & Weber, J. K. R. Structure of molten titanium dioxide. *Phys. Rev. B* **90**, 094204 (2014).

59. Alderman, O. L. G., Benmore, C. J., Neuefeind, J., Tamalonis, A. & Weber, R. Molten barium titanate: A high-pressure liquid silicate analogue. *J. Phys. Condens. Matter* **31**, 20LT01 (2019).

60. King, S. V. Ring Configurations in a Random Network Model of Vitreous Silica. *Nature* **213**, 1112–1113 (1967).
61. Roux, S. Le. Atomes. https://atomes.ipcms.fr/ (2023).
62. Kresse, G. & Furthmüller, J. Efficient iterative schemes for ab initio total-energy calculations using a plane-wave basis set. *Phys. Rev. B* **54**, 11169–11186 (1996).
63. Kresse, G. & Joubert, D. From ultrasoft pseudopotentials to the projector augmented-wave method. *Phys. Rev. B* **59**, 1758–1775 (1999).
64. Perdew, J. P., Burke, K. & Ernzerhof, M. Generalized Gradient Approximation Made Simple. *Phys. Rev. Lett.* **77**, 3865–3868 (1996).
65. Chen, J.-L. & Kaltsoyannis, N. DFT + U Study of Uranium Dioxide and Plutonium Dioxide with Occupation Matrix Control. *J. Phys. Chem. C* **126**, 11426–11435 (2022).
66. Liechtenstein, A. I., Anisimov, V. I. & Zaanen, J. Density-functional theory and strong interactions: Orbital ordering in Mott-Hubbard insulators. *Phys. Rev. B* **52**, R5467–R5470 (1995).
67. Wang, H. & Konashi, K. LDA+U study of Pu and PuO2 on ground state with spin–orbital coupling. *J. Alloys Compd.* **533**, 53–57 (2012).
68. Cooper, M. W. D. *et al.* Development of Xe and Kr empirical potentials for CeO2, ThO2, UO2 and PuO2, combining DFT with high temperature MD. *J. Phys. Condens. Matter* **28**, 405401 (2016).
69. Grimme, S., Antony, J., Ehrlich, S. & Krieg, H. A consistent and accurate ab initio parametrization of density functional dispersion correction (DFT-D) for the 94 elements H-Pu. *J. Chem. Phys.* **132**, 154104 (2010).
70. Grimme, S., Ehrlich, S. & Goerigk, L. Effect of the damping function in dispersion

corrected density functional theory. *J. Comput. Chem.* **32**, 1456–1465 (2011).

71. Bartók, A. P., Kondor, R. & Csányi, G. On representing chemical environments. *Phys. Rev. B* **87**, 184115 (2013).

72. Deringer, V. L. & Csányi, G. Machine learning based interatomic potential for amorphous carbon. *Phys. Rev. B* **95**, 94203 (2017).

73. Sivaraman, G. *et al.* Machine-learned interatomic potentials by active learning: amorphous and liquid hafnium dioxide. *npj Comput. Mater.* **6**, 104 (2020).

74. Sivaraman, G. *et al.* Automated Development of Molten Salt Machine Learning Potentials: Application to LiCl. *J. Phys. Chem. Lett.* **12**, 4278–4285 (2021).

75. Guo, J. *et al.* Composition-transferable machine learning potential for LiCl-KCl molten salts validated by high-energy x-ray diffraction. *Phys. Rev. B* **106**, 14209 (2022).

76. Guo, J. *et al.* AL4GAP: Active learning workflow for generating DFT-SCAN accurate machine-learning potentials for combinatorial molten salt mixtures. *J. Chem. Phys.* **159**, 24802 (2023).

77. Cooper, M. W. D., Rushton, M. J. D. & Grimes, R. W. A many-body potential approach to modelling the thermomechanical properties of actinide oxides. *J. Phys. Condens. Matter* **26**, 105401 (2014).

78. Cooper, M. W. D., Murphy, S. T., Fossati, P. C. M., Rushton, M. J. D. & Grimes, R. W. Thermophysical and anion diffusion properties of (Ux,Th1-x)O2. *Proc. R. Soc. A Math. Phys. Eng. Sci.* **470**, 20140427 (2014).

79. Plimpton, S. Fast Parallel Algorithms for Short-Range Molecular Dynamics. *J. Comput. Phys.* **117**, 1–19 (1995).

80. Csányi, G. *et al.* Expressive programming for computational physics in Fortran 95+. *IoP*

Comput. Phys. Newsl. (2007).

81. Nosé, S. A unified formulation of the constant temperature molecular dynamics methods. *J. Chem. Phys.* **81**, 511–519 (1984).

82. Hoover, W. G. Canonical dynamics: Equilibrium phase-space distributions. *Phys. Rev. A* **31**, 1695–1697 (1985).

Acknowledgements. This work was supported by the U.S. Department of Energy (DOE) through grants DE-SC0018601 and DE-SC0015241 and the Argonne Laboratory Directed Research and Development program. X-ray diffraction measurements were made at Sector 6-ID-D of the Advanced Photon Source, a U.S. DOE Office of Science User Facility, operated by Argonne National Laboratory under Contract No. DE-AC02-06CH11357. The authors gratefully acknowledge John Vacca, Lynn Soderholm, Wendy VanWingeren and Elizabeth Schmidt for technical advice and safety management contributions that enabled the X-ray measurements, Mark Schvaneveldt for assembling the sample chamber, Andrew Hebden for sample chamber design considerations, and Steve Salbeck, Hadco Tool, LLC, for advice and fabrication of sample handling, nozzle housing, and sample die components.

Author contributions. C.J.B., O.L.G.A., M.A.W., and R.W. conceived the idea for X-ray diffraction measurements and developed the sample chamber with A.T. O.L.G.A. wrote the proposal for X-ray beamtime. S.K.W., C.J.B., and R.W. conducted the X-ray measurements. S.K.W. analyzed the X-ray data and performed the empirical potential structure refinements with guidance from C.J.B., O.L.G.A., and R.W. G.S. developed the Gaussian approximation potential from density functional theory calculations and performed molecular dynamics simulations,

673 under guidance of D.A.A. M.D.R. and K.L.H. prepared the PuO_2 samples and facilitated
674 radioactive sample handling under the guidance of M.A.W. S.K.W. prepared the manuscript
675 draft, with revisions contributed by all.
676
677 **Competing interests.** The authors declare no competing interests.
678
679 **Additional information**
680 **Supplementary information** is available for this paper at [URL].
681 **Correspondence and requests for materials** should be addressed to Stephen Wilke.
682 **Peer review information.** [TBD]
683 **Reprints and permissions information** is available at http://www.nature.com/reprints.
684
685
686

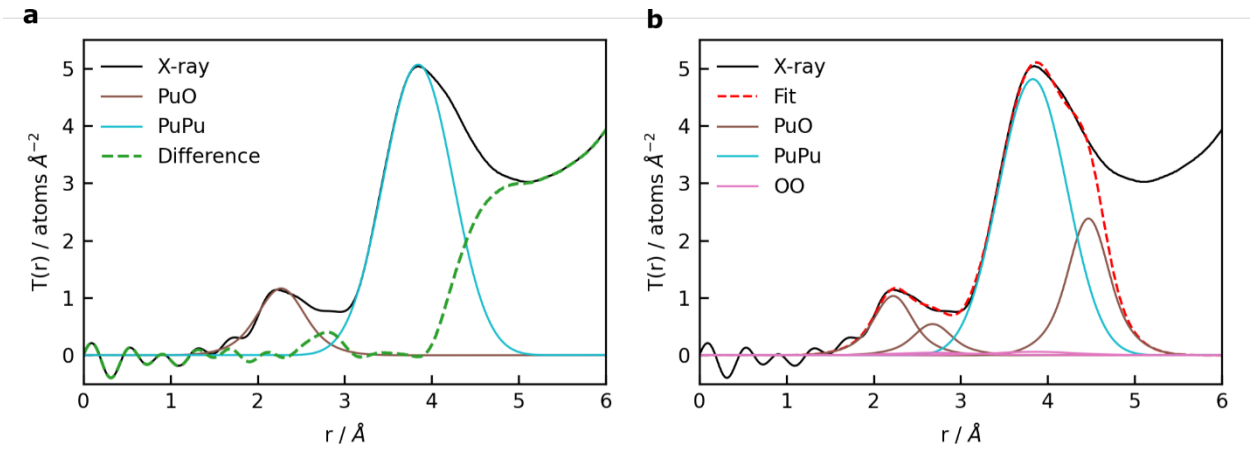

687

688 **Extended Data Fig. 1. Fitting of Gaussian distributions to the total PDF for molten $PuO_{1.76}$.**

689 **a,** Fitting a single PuO distribution to the leading edge of the first peak, and a single PuPu

690 distribution to the leading edge of the second peak. **b,** Optimized peak fitting for all pair

691 correlations, guided by the bond distances and coordinations anticipated from *f*-PuO_2 and α-

692 Pu_2O_3 crystal structures.

693

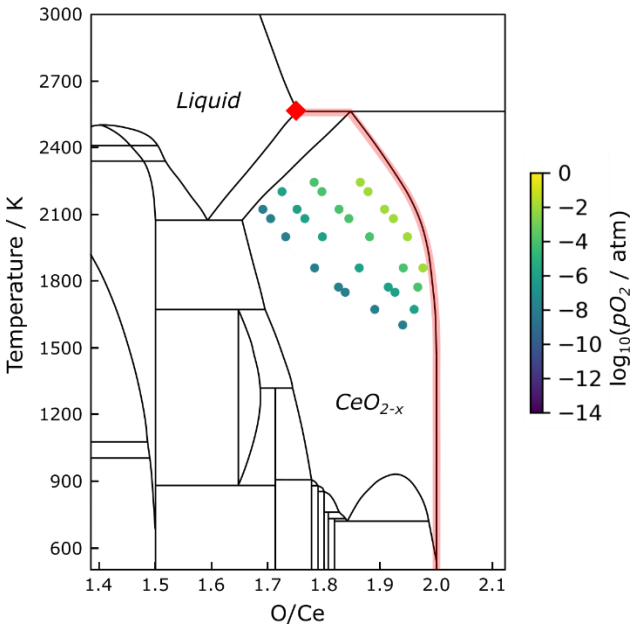

694

695 **Extended Data Fig. 2. Ce-O phase diagram**. Colored markers show oxygen gas partial

696 pressure (pO_2) isobars[33]. The redox trajectory for a sample heated under pure O_2 is shaded in

697 pink.

698

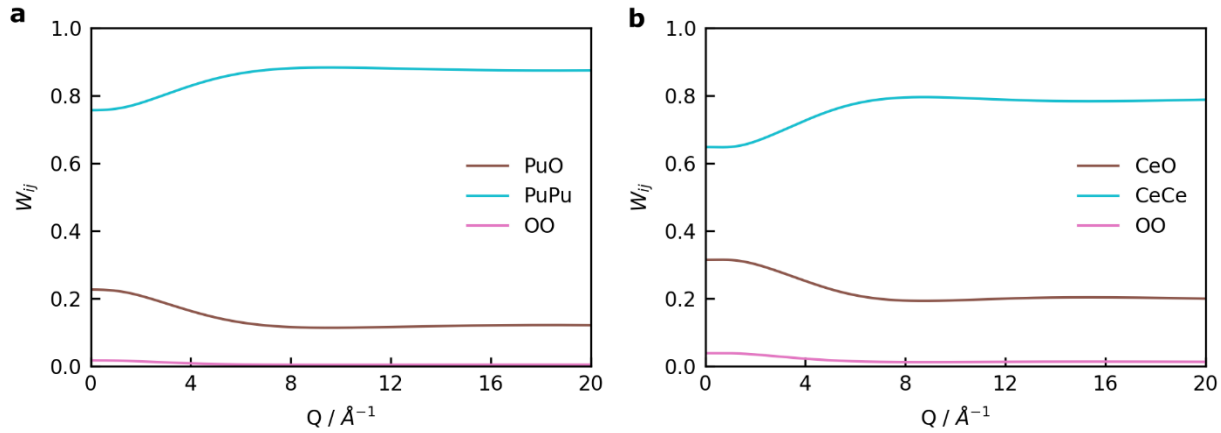

699

700 **Extended Data Fig. 3. Faber-Ziman X-ray weighting factors. a,** $PuO_{1.76}$. **b,** $CeO_{1.75}$. From

701 Eqn. 2.

702

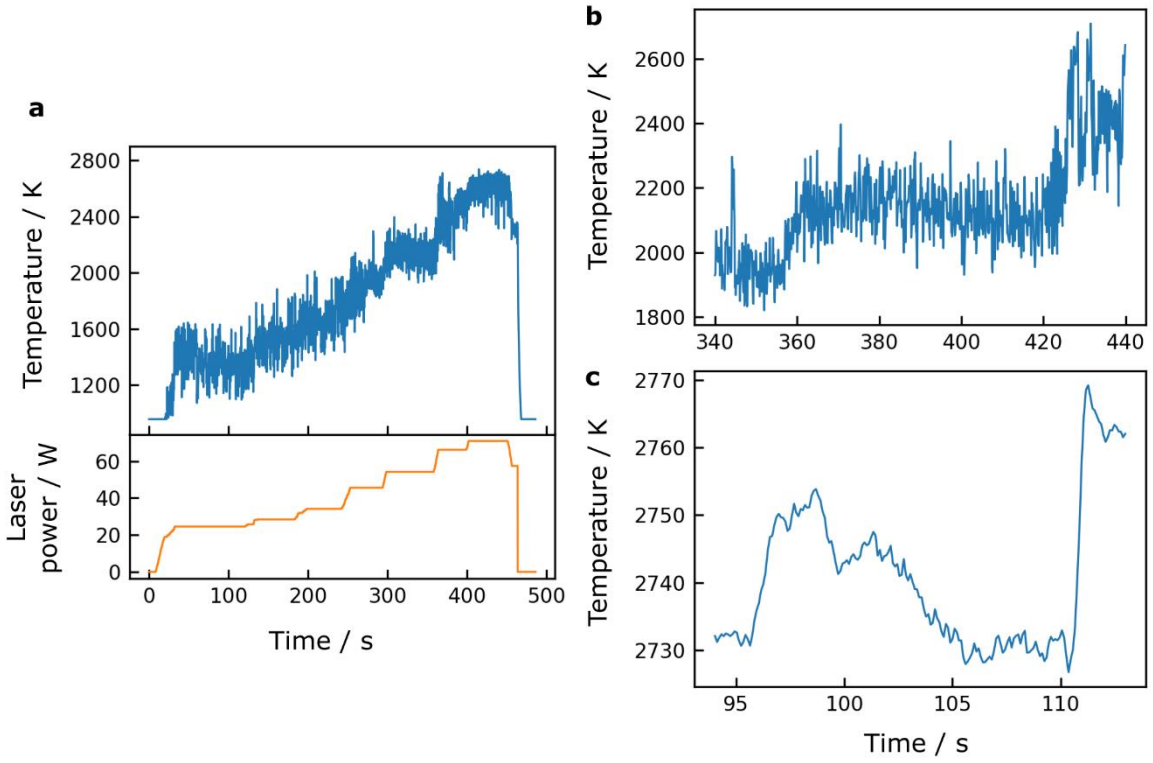

703

704 **Extended Data Fig. 4. Examples of sample temperature during levitation and laser beam**

705 **heating. a,** Emissivity-corrected temperature measurements (10 Hz acquisition) from the optical

706 pyrometer for PuO_{2-x} solid heated under 5% CO (Ar balance). Laser power was increased

707 incrementally, interspersed with X-ray diffraction measurements taken while the sample was

708 held isothermally. **b,** Zoomed-in view of a single isotherm from (**a**). For the time period 364-416

709 s, the temperature mean was 2140 K with a standard deviation of 71 K. **c,** Temperature of molten

710 $PuO_{1.57}$ during a different heating run than (**a-b**). X-ray measurements were analyzed for the time

711 period 105-110 s, which had a temperature mean of 2730 K and a standard deviation of 2 K.

712

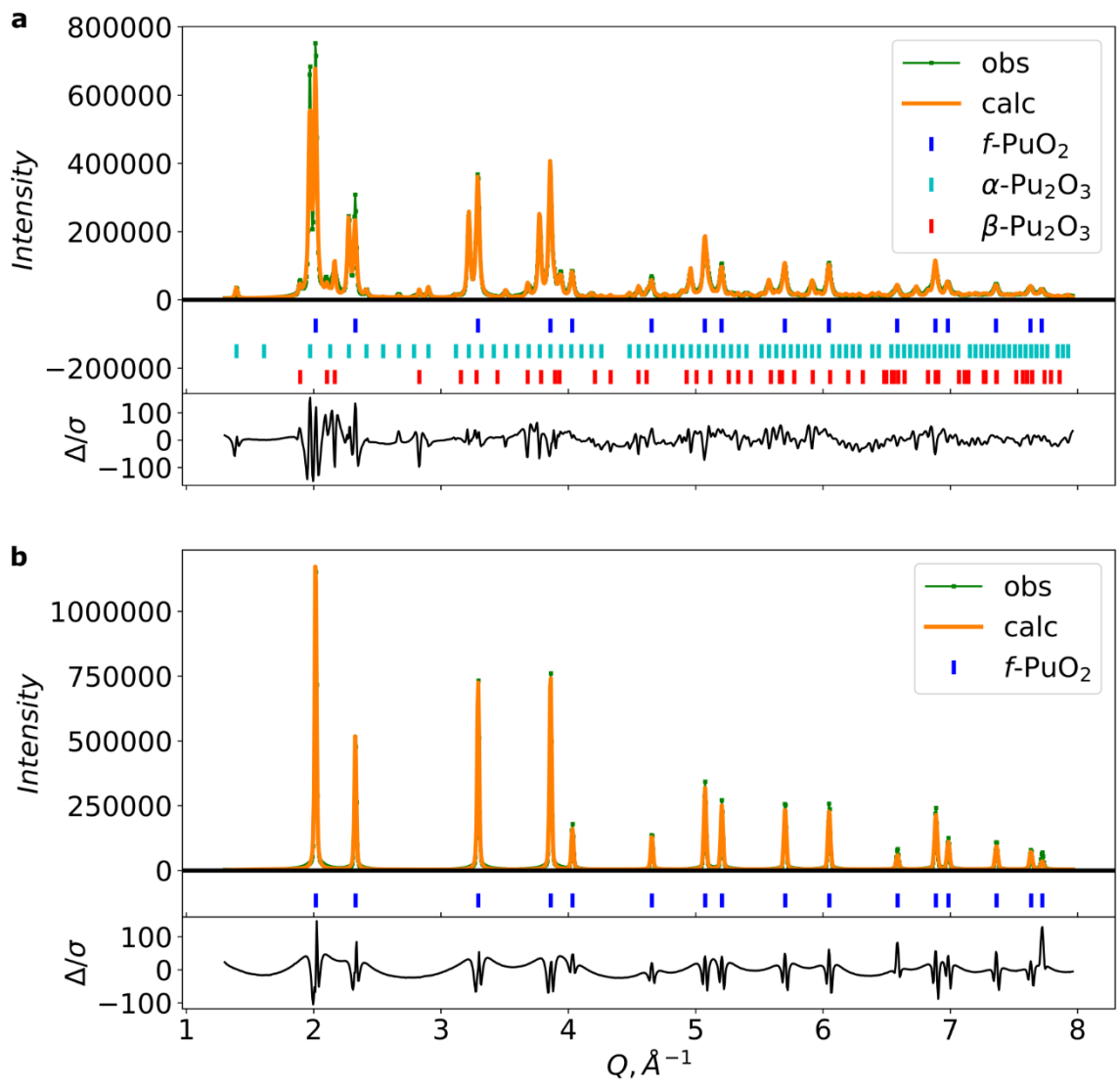

713

714 **Extended Data Fig. 5. X-ray diffraction and Rietveld refinements for selected crystalline**

715 **samples. a,** Initial Pu-O material before heating. **b,** Pure *f*-PuO_2 after heating under O_2. The

716 observed X-ray diffraction patterns (green curves) and calculated Rietveld refinement models

717 (orange curves) are compared against the Bragg reflections for *f*-PuO_2, α-Pu_2O_3, and β-Pu_2O_3

718 (blue, teal, and red vertical ticks). The black curves show the differences between the X-ray data

719 and refinement models, divided by the estimated standard uncertainties.

720

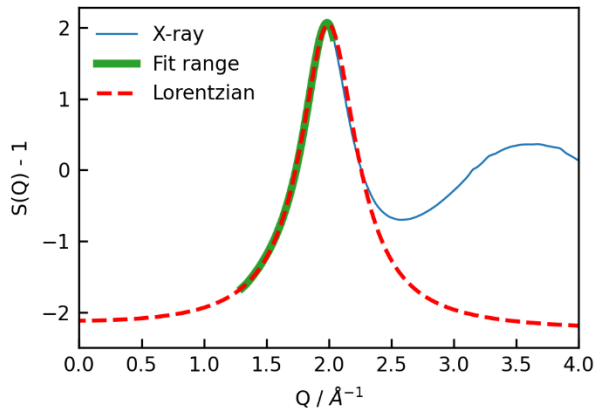

Extended Data Fig. 6. Fitting of a Lorentzian function to the structure factor's first principal peak, for molten $PuO_{1.76}$. The fit[54] includes the Lorentzian contribution mirrored across $Q = 0$ Å^{-1} and is constrained[17] to $S(0) = 1 - \langle f(0)^2 \rangle / \langle f(0) \rangle^2$ = -1.113. The X-ray diffraction data were extrapolated to $Q = 0$ using this Lorentzian fit, prior to the Fourier transform to obtain the PDFs (Eqn. 3-4).

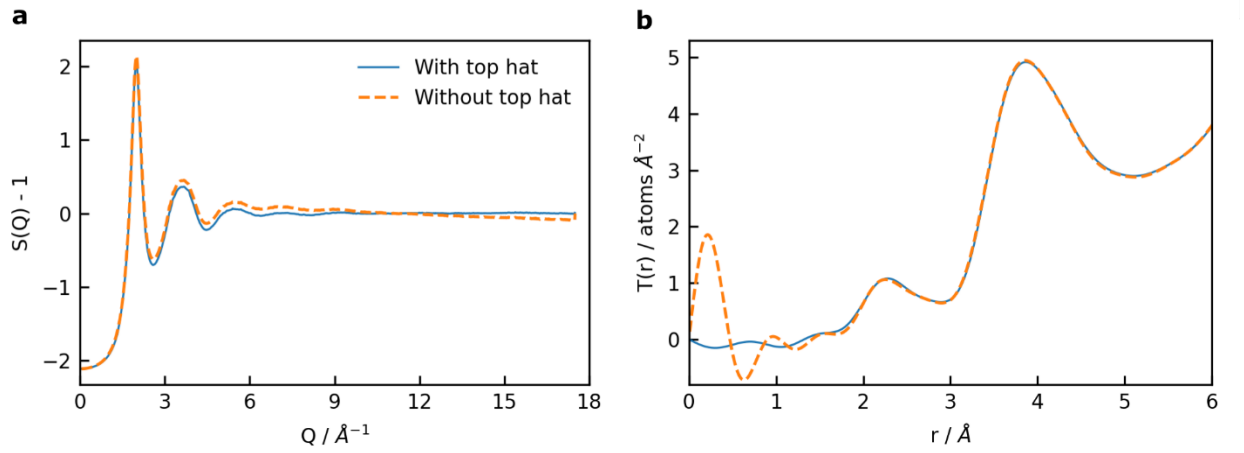

728

729 **Extended Data Fig. 7.** Effect of top hat convolution on X-ray data. Comparison of the (a) X-ray

730 structure factor and (b) total PDF for molten $PuO_{1.76}$, processed with and without the top hat

731 convolution[55] in GudrunX. For this comparison, Q_{max} = 11.9 Å^{-1} was used for both structure

732 factors to avoid large truncation oscillations in the PDF without top hat.

733

Extended Data Table 1. Faber-Ziman weighting factors. For Q = 0 Å^{-1}; M = Pu or Ce. According to Eqn. 2, expressed in percent.

	$PuO_{1.57}$	**$PuO_{1.69}$**	**$PuO_{1.76}$**	**$CeO_{1.75}$**
W_{MO}	20.78	21.98	22.63	31.33
W_{MM}	77.83	76.44	75.68	64.89
W_{OO}	1.39	1.58	1.69	3.78